ASC Report No. 21/2017

Some two-dimensional multiscale finite element formulations for the eddy current problem in iron laminates

K. Hollaus, and J. Schöberl

Institute for Analysis and Scientific Computing
Vienna University of Technology — TU Wien
www.asc.tuwien.ac.at ISBN 978-3-902627-00-1

Most recent ASC Reports

20/2017 *E. Daus, L. Desvillettes, and A. Jüngel*
Cross-diffusion systems and fast-reaction limits

19/2017 *A. Jüngel*
Cross-diffusion systems with entropy structure

18/2017 *A. Arnold, A. Einav and T. Wöhrer*
On the rates of decay to equilibrium in degenerate and defective Fokker-Planck equations

17/2017 *C. Erath and D. Praetorius*
Adaptive vertex-centered finite volume methods for general second-order linear elliptic PDEs

16/2017 *A. Jüngel, and O. Leingang*
Blow-up of solutions to semi-discrete parabolic-elliptic Keller-Segel models

15/2017 *H. de Snoo, H. Woracek*
The Krein formula in almost Pontryagin spaces.
A proof via orthogonal coupling

14/2017 *W. Auzinger, I. Brezinova, H. Hofstätter, O. Koch, M. Quell*
Practical splitting methods for the adaptive integration of nonlinear evolution equations.
Part II: Comparison of local error estimation and step-selection strategies for nonlinear Schrödinger and wave equations

13/2017 *L. Banjai, J.M. Melenk, R.H. Nochetto, E. Otarola, A. Salgado, and C. Schwab*
Tensor FEM for spectral fractional diffusion

12/2017 *S. Börm, C. Börst, J.M. Melenk*
An analysis of a butterfly algorithm

11/2017 *X. Chen and A. Jüngel*
A note on the uniqueness of weak solutions to a class of cross-diffusion styles

Institute for Analysis and Scientific Computing
Vienna University of Technology
Wiedner Hauptstraße 8–10
1040 Wien, Austria

E-Mail: admin@asc.tuwien.ac.at
WWW: http://www.asc.tuwien.ac.at
FAX: +43-1-58801-10196

ISBN 978-3-902627-00-1

Some Two-Dimensional Multiscale Finite Element Formulations for the Eddy Current Problem in Iron Laminates

K. Hollaus, and J. Schöberl
Institute for Analysis and Scientific Computing, Vienna University of Technology,
Wiedner Hauptstraße 8-10, A-1040 Wien, Austria, karl.hollaus@tuwien.ac.at

***Abstract*—The aim of this work is to introduce and to study the performance of some multiscale finite element formulations for the eddy current problem in laminated iron in two dimensions. The case of the main magnetic flux parallel to the laminates and perpendicular to the plane of projection is considered. Multiscale approaches based on the magnetic vector potential (MVP), the single component current vector potential (SCCVP) and on a mixed formulation are presented. An approach for a multiscale formulation (MSF) with the MVP is constructed at the best by examining and representing the eddy current distribution in laminated iron of a reference solution. The associated weak form of the multiscale finite element method (MSFEM) is presented. Similarly to the MVP the SCCVP and a mixed formulation with the MVP and the current density are studied.**

This work does not present a mathematical analysis of MSFEM for eddy currents in laminates. The performance of MSFEM is studied by numerous numerical experiments of different examples. The paper covers the topics edge effect, averaging of coefficients and p-refinement of multiscale shape-functions and of standard finite element polynomials (SFEPs) and stability of MSFEM in a particular case.

Simulations show the capability of MSFEM to efficiently and accurately approximate eddy currents in iron laminates. The simulations shall also provide a collection of numerical examples to evaluate other multiscale or homogenization methods.

***Index Terms*—Eddy currents in 2D, edge effect, generalized finite element method GFEM, laminated iron cores, micro-shape function, multiscale formulation MSF, multiscale finite element method MSFEM, p-refinement, linear dependence.**

I. Introduction

The discretization of the micro-structure of laminated iron cores i.e. of each laminate by finite elements (FEs) would lead to prohibitively large systems of equations, whose solution is far away from being a routine task for engineers in the design of electrical devices with modern computer power or even impossible. To overcome this unpleasant fact homogenization and multiscale methods have been developed, which require basically the solution of the large scale problem.

A homogenization method has been proposed in [1] with averaging the material properties for static magnetic fields in laminates in two dimensions.

Homogenization methods based on a truncated asymptotic expansion as an approach for the solution of the eddy current problem (ECP) lead to an average value and corrector terms, see for instance [2] or [3]. An asymptotic expansion with the MVP $\boldsymbol{A}$ was used in [4]. To improve the local approximation first and second order corrector terms were determined in [5] solving associated cell problems for the SCCVP T in two dimensions.

A multiscale method has been presented in [6]. The magnetic flux density parallel to the lamination is expanded into orthogonal even polynomials, so-called orthogonal skin effect sub-basis functions, to improve the local approximation. The arising coefficients are averaged and the edge effect is neglected.

The present paper deals with multiscale finite element methods (MSFEMs) and possibly applies averaging of the coefficients. Some two-dimensional multiscale finite element formulations are introduced and analyzed. Simulations of small and simple numerical examples and of a more demanding large and nonlinear one are carried out to study the performance of the proposed MSFEMs with respect to different parameters, for example, the penetration depth. Solutions with MSFEM are compared with reference solutions (RS) [7] where each laminate is modeled by FEs.

Section II gives an introduction to MSFEM in the context of eddy currents in laminated media. The boundary value problem of the eddy current problem to be solved is described in Sec. III. Details of the small numerical examples are summarized in Sec. IV. All topics mentioned in the following are supplemented by numerical experiments. The multiscale finite element formulation with $\boldsymbol{A}$ is presented in Sec. V. A physically motivated explanation of the approach for a MSF is given by the eddy current distribution in laminates. How to construct a MSF by means of a RS for $\boldsymbol{A}$ is discussed in detail. Coefficients haven't been averaged for the sake of accuracy, except in Sec. V-E and V-F where the influence of averaging is investigated and the possibility to use triangular meshes is demonstrated, respectively. The behavior of MSFEM concerning p-refinement of the micro-shape functions (MSFs), the power of higher order MSFEM (HMSFEM), is studied in sections V-G. Stability of MSFEM with respect to the degree of SFEPs in a particular case is addressed in Sec. V-H. A large and nonlinear problem has been studied to demonstrate the ability of the MSFEM to cope with nonlinear problems and show the benefit compared with the standard finite element method (SFEM) in Sec. VI. MSFEM for the SCCVP T is shown in Sec. VII. The behavior of MSFEM concerning p-refinement of the SFEP bases [8] is studied in

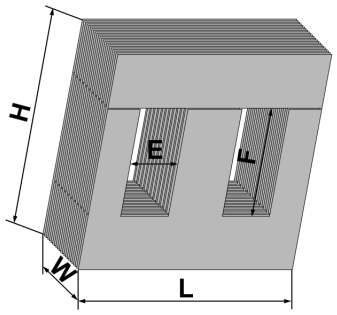

Figure 1: Transformer core with large scale dimensions L etc.

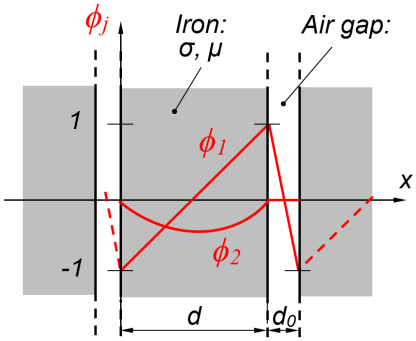

Figure 2: Small scale dimensions, d+d_0 represents one periode, micro-shape functions ϕ_i.

VII-E. The improvement of the accuracy increasing the degree of the SFEPs is investigated. Attention is paid to the edge effect in VII-F. Finally, a mixed MSF using the $\boldsymbol{A}$ and the current density $\boldsymbol{J}$ is introduced in Sec. VIII.

II. Multiscale Finite Element Method MSFEM

The problem we are confronted with exhibits two different scales. A large scale characterized by large scale dimensions, for instance the length L, the height H, the width W and the dimensions of the windows, E and F, of a transformer core shown in Fig. 1. The thickness d of the laminates, the width of the air gap d_0 in between the laminates, see Fig. 2, and the penetration depth δ are dimensions at the small scale or at the micro-scale. The ratio of the different scales is extremely large, about 10^5 up to 10^6.

Mapped polynomials are used by the standard finite element method (SFEM) to approximate the unknown solution. The SFEM performs well as long as the solution or the coefficients in the equations are smooth. However, to obtain an accurate approximation also in case of equations with rough coefficients, for instance materials with a micro-structure (laminated iron core) or for problems with singularities like boundary layers, extremely fine meshes are required [9]. This is the reason for the prohibitively large equation systems which may require exorbitant amounts of computer resources to obtain an accurate solution [10]. This work addresses solely the eddy current problem in 2D with rough coefficients because of a laminated iron core.

To avoid large algebraic equation systems the generalized finite element method (GFEM) as a general framework for equations with rough coefficients or for problems with singularities seems to be a very promising option [9], [10]. Apart from the finite dimensions laminated iron cores represent a problem with a periodic micro-structure. The SFEP basis is augmented by special functions including a priori information into the ansatz space

$$u_h(x) = \sum_{i=1}^{n}\sum_{j=1}^{m} u_{ij}\varphi_i(x)\phi_j(x) = \sum_{i=1}^{n}\sum_{j=1}^{m} u_{ij}\psi_{ij}(x), \qquad (1)$$

where n is the number of the SFEPs φ_i, m is the number of special functions ϕ_j and u_{ij} are the coefficients of the approximate solution u_h. The special functions, which are custom tailored ansatz functions, may stem from an analytic solution or, for example, from a FE solution of a basic problem, i. e. these functions are known. The local basis of the special functions approximates well the solution locally. Micro-shape functions ϕ_j represent a local space and standard polynomials $\varphi_i(x)$ a global space. Multiplication of standard polynomials φ_i with special functions ϕ_j yields the new basis functions ψ_{ij}.
In the present context of micro- and macro-scale we call the method MSFEM and the special functions ϕ_j the micro-shape functions, see Fig. 2.

III. Eddy Current Problem

The simplified eddy current problem (ECP) in two dimensions to be solved in the present work is shown in Fig. 3. The entire domain $\Omega = \Omega_m \cup \Omega_0$ consists of the laminated medium Ω_m and air Ω_0, Ω_m comprises laminates Ω_c, i.e. the conducting domain, and air gaps in between. Eddy currents represented by the current density $\boldsymbol{J}$ occur in Ω_c. The interface Γ_{m0} separates Ω_m from Ω_0. The outer boundary of Ω is denoted by Γ and $\boldsymbol{n}$ is the unit normal vector pointing out of Ω. The magnetic flux density $\boldsymbol{B}$ is assumed to be parallel to the laminates and perpendicular to the plane of projection. The material parameters are the magnetic permeability $\mu(\boldsymbol{B})$, which can be nonlinear, and the electric conductivity σ. Relations (2) to (6) are valid in Ω_c, whereas (7) to (9) belong to air Ω_0 including the air gaps in Ω_m and (10, 11) are possible

$$\operatorname{curl}\boldsymbol{H} = \boldsymbol{J} \quad \text{in } \Omega_m \qquad (2)$$
$$\operatorname{curl}\boldsymbol{E} = -\tfrac{\partial}{\partial t}\boldsymbol{B} \qquad (3)$$
$$\operatorname{div}\boldsymbol{B} = 0 \qquad (4)$$
$$\boldsymbol{J} = \sigma\boldsymbol{E} \qquad (5)$$
$$\boldsymbol{B} = \mu\boldsymbol{H} \qquad (6)$$

$$\operatorname{curl}\boldsymbol{H} = \boldsymbol{J}_0 \quad \text{in } \Omega_0 \qquad (7)$$
$$\operatorname{div}\boldsymbol{B} = 0 \qquad (8)$$
$$\boldsymbol{B} = \mu\boldsymbol{H} \qquad (9)$$

$$\boldsymbol{H}\times\boldsymbol{n} = \boldsymbol{K} \quad \text{on } \Gamma_H \qquad (10)$$
$$\boldsymbol{B}\cdot\boldsymbol{n} = b \quad \text{on } \Gamma_B \qquad (11)$$

boundary conditions on Γ. The boundary value problem BVP (2) to (11) considers Dirichlet boundary conditions only. The BVP of the ECP in the frequency domain is straightforward and thus not shown here.

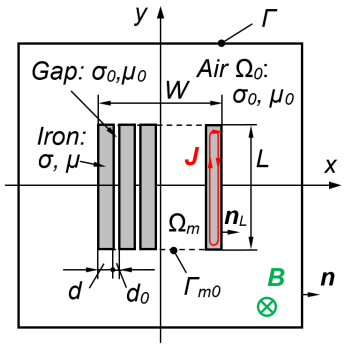

Figure 3: Problem in 2D.

IV. Numerical Simulations

A. Relative errors in percentage

To evaluate the performance of MSFEM with respect to for instance the penetration depth δ relative errors of the potential u, the flux density $\operatorname{curl} u$ and the eddy current losses P,

$$\frac{\|u_{MSFEM}-u_{RS}\|_{L_2}}{\|u_{RS}\|_{L_2}}\cdot 100\%,\quad \frac{\|\operatorname{curl}(u_{MSFEM})-\operatorname{curl}(u_{RS})\|_{L_2}}{\|\operatorname{curl}(u_{RS})\|_{L_2}}\cdot 100\% \quad \text{and} \quad \frac{P_{MSFEM}-P_{RS}}{P_{RS}}\cdot 100\%, \tag{12}$$

respectively, are computed by means of a RS and that of MSFEM. Single laminates are modeled by FEs for the RS. Errors (12) are evaluated in Ω_c, i.e. iron laminates, only. The frequency was changed to get different δ.

B. Finite element models

A small example has been deliberately chosen to demonstrate also errors which would not be visible in large problems by means of (12). All data are given so that the simulation results can be verified. The problem is symmetric with respect to both axes, x and y, assuming the origin in the center of the problem domain, compare with Fig. 3. The dimensions of the domains are $|\Omega_m| = 20\times 20$ mm^2 and $|\Omega| = 40\times 40$ mm^2. The FE models shown in Figs. 4 for the RS and for MSFEM consider 10 laminates, $d = 1.8$mm, and air gaps in between, $d_0 = 0.2$mm. For meaningful errors (12) the discretization in y-direction is the same for both FE models. The dimensions of the FE models in Figs. 4 are summarized in Table I.
The fill factor $f_f = \frac{d}{d+d_0}\cdot 100$ of 90% is valid for all examples. In case of averaging $d + d_0 = 0.5$ mm was selected. Most of the simulations use the models with dimensions summarized in Tab. I.

V. Multiscale Finite Element Formulation with $\boldsymbol{A}$

In brief, the time domain is only presented here. In case of linear material properties the problem is formulated in the frequency domain with the phasor convention $e^{j\omega t}$.

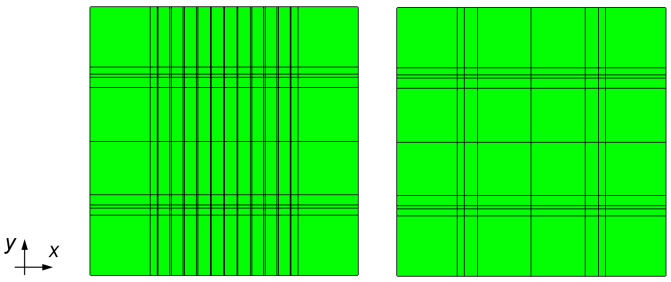

Figure 4: FE models for a) RS (left) and b) MSFEM (right).

Table I: Dimensions of the FE Models in mm [a]

Δ x, RS	9	1	0.1	1.8	0.2 ... [b]
Δ x, MSFEM	9	1	2	8	
Δ y	9	1	0.5	1.5	8

[a] Due to the symmetry only one half of the dimensions in x- and y-direction are presented.
[b] After 10 laminates with air gaps in between the dimensions repeat accordingly to obtain a symmetric problem.

A. Boundary value problem with $\boldsymbol{A}$

The magnetic vector potential (MVP) $\boldsymbol{A}$ is introduced by $\boldsymbol{B} = \operatorname{curl}\boldsymbol{A}$ with

$$\boldsymbol{A}: \quad \Omega\subset\mathbb{R}^2\to\mathbb{K}^2, \qquad (x,y)\mapsto (A_1(x,y),A_2(x,y))^T \tag{13}$$

$$\operatorname{curl}\boldsymbol{A}: \quad \Omega\subset\mathbb{R}^2\to\mathbb{K}, \qquad (x,y)\mapsto \left(\frac{\partial A_2}{\partial x}-\frac{\partial A_1}{\partial y}\right)(x,y) \tag{14}$$

where $\mathbb{K}$ stands either for real numbers $\mathbb{R}$ or complex numbers $\mathbb{C}$. Mapping to $\mathbb{R}$ or $\mathbb{C}$ belongs to the time domain or to the frequency domain, respectively. The valid domain is indicated at the given case. Considering the relevant Maxwell's equations leads to the BVP of the ECP in the time domain

$$\operatorname{curl}\frac{1}{\mu(\boldsymbol{A})}\operatorname{curl}\boldsymbol{A}+\sigma\frac{\partial}{\partial t}\boldsymbol{A} = \boldsymbol{0} \quad \text{in } \Omega\subset\mathbb{R}^2, \tag{15}$$

$$\boldsymbol{A}\times\boldsymbol{n} = \boldsymbol{\alpha} \quad \text{on } \Gamma. \tag{16}$$

B. Weak form with $\boldsymbol{A}$

The weak form of the SFEM belonging to the time domain reads:
Find $\boldsymbol{A}_h\in V_{h,\alpha} := \{\boldsymbol{A}_h\in\mathcal{V}_h : \boldsymbol{A}_h\times\boldsymbol{n} = \boldsymbol{\alpha}_h \text{ on } \Gamma\}$, such that

$$\int_\Omega \frac{1}{\mu(\boldsymbol{A}_h)}\operatorname{curl}\boldsymbol{A}_h\cdot\operatorname{curl}\boldsymbol{v}_h\,d\Omega+\frac{\partial}{\partial t}\int_\Omega\sigma\boldsymbol{A}_h\cdot\boldsymbol{v}_h\,d\Omega = 0 \tag{17}$$

for all $\boldsymbol{v}_h\in V_{h,0}$, where $\mathcal{V}_h\subset H(\operatorname{curl},\Omega)$. Index h indicates FE discretization. The solution of (17) serves as RS to evaluate the accuracy of MSFEMs.
Since $\sigma = 0$ in air a regularization by a penalty term [11] was applied to get a unique solution of (17).

C. An approach for the MSF with $\boldsymbol{A}$

There is no rigorous mathematical rule to construct an approach for a MSF. Therefore, in the context of a MVP $\boldsymbol{A}$ the eddy current distribution of a RS in a laminated medium is

studied to devise an approach for the MSF. Figure 5 shows a detail of the RS with eddy currents consisting of a laminar part, currents are flowing parallel to the laminates, up and down in y-direction, and a second part at the end of the laminates, where the eddy currents turn around flowing in x-direction to built closed loops. The later part or this fact is frequently called the "edge effect" in the literature and sometimes neglected [12]. Note, that $\boldsymbol{n}_L$ points into the x-direction as shown in Fig. 3.

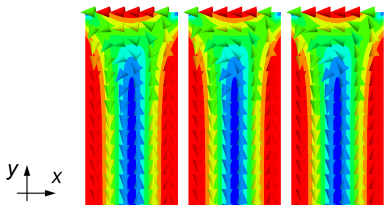

Figure 5: Eddy currents in laminates, detail.

Particular attention is paid to an accurate representation of the edge effect by the MSF in the present work. A separate term considers the edge effect in MSF (18). The first term $\boldsymbol{A}_0$ in (18) takes into account the smooth variations in the solution due to the large scale dimensions and the second and third term consider the solution due to the micro-structure. The second term is a vector with the component A_1 in the y-direction modeling the laminar part of the eddy currents and the third term with $(w_1\phi_1)$ considers the edge effect. The tilde in (18) indicates MSF. The zig-zag function ϕ_1 is the micro-shape function which fits to the periodic micro-structure as depicted in Fig. 2. Maximum and minimum are selected arbitrarily, the choice 1 and -1 is convenient. The micro-shape function is periodic, continuous across the lamination and known. The selection of ϕ_1 stems from the linear approximation of the analytic solution of eddy currents in an infinite slab where $\boldsymbol{B}$ is parallel to the slab with the MVP. Without the third term in (18) for the edge effect the associated MSFEM does not work at all.

$$\tilde{\boldsymbol{A}} = \boldsymbol{A}_0 + \phi_1 \begin{pmatrix} 0 \\ A_1 \end{pmatrix} + \nabla(\phi_1 w_1) \tag{18}$$

The support of the MSF (18) is depicted in Fig. 6, $\boldsymbol{A}_0$ is valid in the entire domain Ω, whereas A_1 and w_1 are restricted to the laminated domain Ω_m.

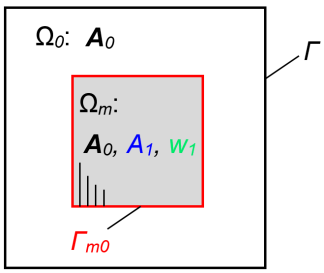

Figure 6: Support, boundary and interface conditions.

D. Weak form of MSFEM with $\boldsymbol{A}$

Simply speaking replacing $\boldsymbol{A}$ in the weak form (17) of the primary formulation by MSA (18) yields the weak form of MSFEM with $\tilde{\boldsymbol{A}}$:
Find $(\boldsymbol{A}_{0h}, A_{1h}, w_{1h}) \in V_{h,\alpha} := \{(\boldsymbol{A}_{0h}, A_{1h}, w_{1h}) : \boldsymbol{A}_{0h} \in \mathcal{U}_h, A_{1h} \in \mathcal{V}_h\ ,\ w_{1h} \in \mathcal{W}_h$ and $\boldsymbol{A}_{0h} \times \boldsymbol{n} = \boldsymbol{\alpha}_h$ on $\Gamma\}$, such that

$$\int_\Omega \frac{1}{\mu} \operatorname{curl} \tilde{\boldsymbol{A}}_h \cdot \operatorname{curl} \tilde{\boldsymbol{\nu}}_h \, d\Omega + \frac{\partial}{\partial t} \int_\Omega \sigma \tilde{\boldsymbol{A}}_h \cdot \tilde{\boldsymbol{\nu}}_h \, d\Omega = 0 \tag{19}$$

for all $(\boldsymbol{\nu}_{0h}, \nu_{1h}, q_{1h}) \in V_{h,0}$, where $\mathcal{U}_h$ is a FE subspace of $H(\operatorname{curl}, \Omega)$, $\mathcal{V}_h$ of $L_2(\Omega_m)$, $\mathcal{W}_h$ of $H^1(\Omega_m)$ and ϕ_1 is in the space of periodic and continuous functions $H^1_{per}(\Omega_m)$. The MSFEM with $A_1 \in H^1(\Omega_m)$ is analyzed in Sec. V-F.
Dirichlet boundary conditions are prescribed for $\boldsymbol{A}_{0h}$ on Γ and homogenous natural boundary conditions hold for w_1 and for A_1 in Γ_{m0}.
The FE approximation of the MSF (18) is consistent with the $H(\operatorname{curl})$ space. A FE subspace of $H(\operatorname{curl}, \Omega)$ is selected for the first term $\boldsymbol{A}_{0h}$. The x-dimension of the rectangular FEs is assumed to be an integer multiple of the period $p = d + d_0$ and $\phi_1 = 0$ along the relevant FE boundaries. This means that the second term is tangentially continuous across the laminates. The third term is a gradient of continuous functions. Thus, the latter two belong also to FE subspaces of $H(\operatorname{curl}, \Omega_m)$.
Solutions of $\boldsymbol{A}_{0h}$, A_{1h} and w_{1h} are very smooth as can be seen in Figs. 43 to 44, in Appendix B. Therefore, a rather coarse FE mesh and thus much less unknowns suffice for an accurate approximation of the solutions of MSFEM, see Figs. 4 b) or 23 b). This fact explains the big advantage of MSFEM over SFEM and the RS.

E. Exact integration versus averaging of the coefficients

The ECP in the frequency domain with the complex unit j and the angular frequency ω is considered in this section. The bilinear forms in (19), the curl of gradients vanishes, are written in detail in (20) in Appendix A. Two different numerical techniques to compute the FE matrices are compared, averaging and exact integration, see also [6], [12], [7], [13] and [14].

Averaging of coefficients λ in (19) over the period $p = d + d_0$

$$\overline{\lambda} = \frac{1}{p} \int_0^p \lambda(x) dx, \tag{21}$$

where λ stands for example for $\frac{1}{\mu}$, $j\omega\sigma$, $j\omega\sigma\nabla\phi_1$, $j\omega\sigma\phi_1$, etc., with $\phi_{1x} := \nabla\phi_1$, in (20) in Appendix A, leads to (22) in Appendix A. The averaged coefficients are constant throughout Ω_m. Bilinear forms with averaged coefficients and in turn the weak form are modified. Therefore, all quantities are marked with a bar. Then, the usual Gauss integration of the modified bilinear forms (22) is carried out. The numerical effort is reduced significantly. Quantities of the new weak form are marked with a bar to indicate averaging. This technique clearly implies an error. The solution of the modified weak form with (22) is hopefully as accurate as the original one with (19).

For the exact integration it is assumed that the x-dimension of the rectangular FEs is an integer multiple of p because $\boldsymbol{n}_l$

points into the x-direction, see Fig. 3. Exact integration means that the FEs are split into rectangular subdomains according to d and d_0, respectively, and Gauss integration on the different subdomains is made considering the relevant standard polynomials, micro-shape function and material parameters. The contributions of the integrals over the subdomains are added up for the respective FE matrix.

The errors defined in (12) can be seen in Figs. 7 to 9. There is a significant difference between the RS $\boldsymbol{A}_h$ according to (17) and the MSFEM solution $\tilde{\boldsymbol{A}}_h$ obtained by (19) of the potentials and eddy current losses depending on whether the exact or the averaging integration technique is used. This is clearly visible at small errors due to the logarithmic scaling. The error in $\boldsymbol{A}$ is essentially higher than that of P over the investigated range. The magnetic flux density curl $\boldsymbol{A}$ is hardly affect by the selected integration technique, see Fig. 8. The polynomial degrees of the SFE basis of MSFEM (18) were one for $\boldsymbol{A}_0$ and A_1 and two for w_1. In general errors grow strongly once δ becomes smaller than $d + d_0$ regardless of the integration technique. The HMSFEM in Sec. V-G can solve this problem.

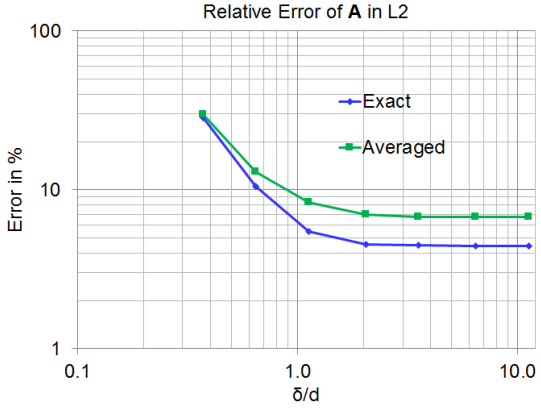

Figure 7: Magnetic vector potential $\boldsymbol{A}$.

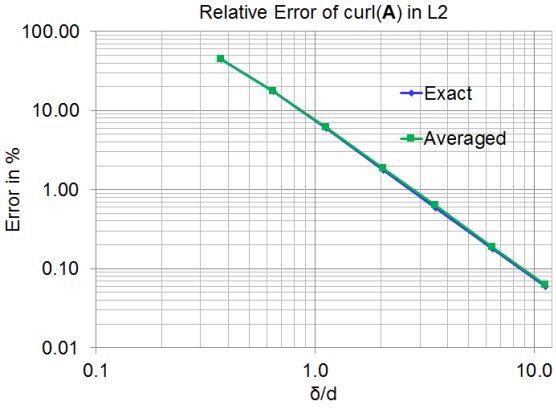

Figure 8: Magnetic flux density curl $\boldsymbol{A}$.

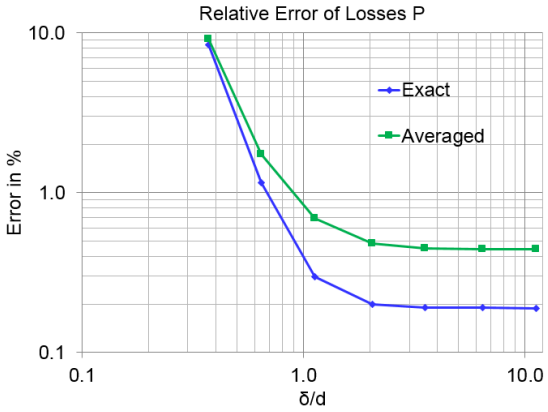

Figure 9: Eddy current losses P.

F. Triangular mesh

MSFEMs with averaged coefficients facilitate an easy use of triangular FE meshes. Two examples are presented in Figs. 10. The computational domain $\Omega_m \cup \Omega_0$ is uniformly subdivided into triangular FEs. The side length of the triangles is approximately s. In case of $s = 20$mm Ω_m consists of only two triangular FEs. All simulations are based on the MSFEM (19) and relation (21).

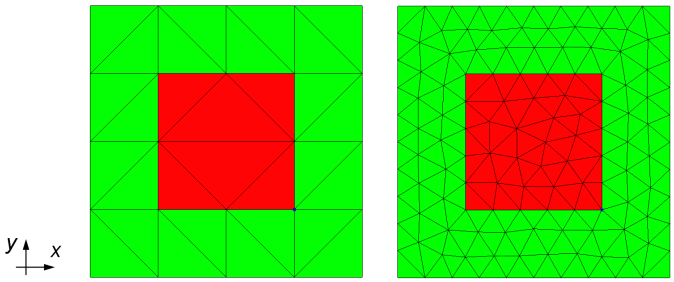

Figure 10: Triangular FE models of $\Omega_m \cup \Omega_0$ in red and green, respectively, with a) $s = 10$mm (left) and b) $s = 4$mm (right).

Eddy current distributions are shown in Figs. 11.

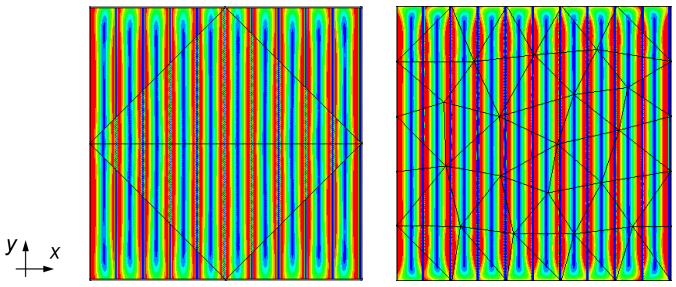

Figure 11: Magnitude of the eddy current density in Ω_m for a) $s = 10$mm (left) and b) $s = 4$mm (right).

The error in $\boldsymbol{A}$ with respect to s is large as can be seen in Fig. 12, the error in curl $\boldsymbol{A}$ is almost independent from s and clearly grows with the frequency (Fig. 13). The limit of the losses P with decreasing s is too small because the

local space is insufficient, see Fig. 14. On the other hand the error grows with s on and on, the insufficiency of the global space becomes significant. The penetration depths are

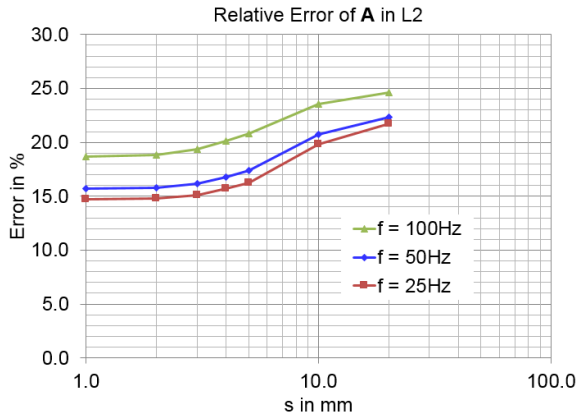

Figure 12: Magnetic vector potential $\boldsymbol{A}$.

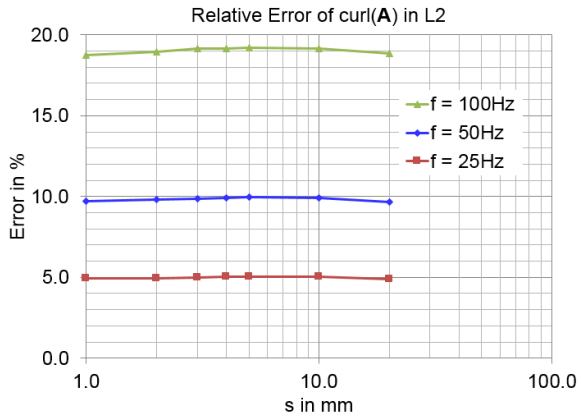

Figure 13: Magnetic flux density curl $\boldsymbol{A}$.

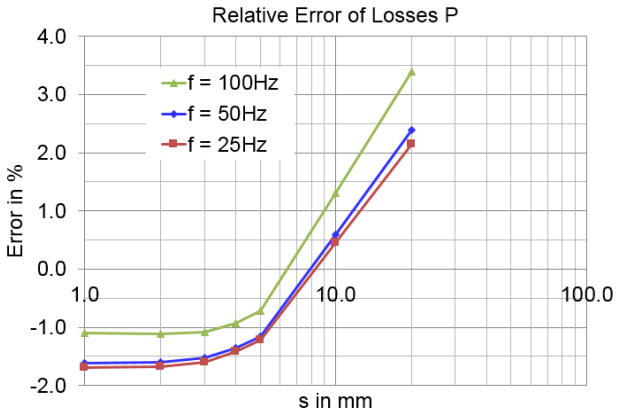

Figure 14: Eddy current losses P.

$\rho_{25} = 2.25$mm, $\rho_{50} = 1.59$mm and $\rho_{100} = 1.13$mm for the frequencies $f = 25$Hz, $f = 50$Hz and $f = 100$Hz, respectively. The width of the laminates is $d = 1.8$mm.

The degree of the SFEPs is one for $\boldsymbol{A}_{0h}$ and A_{1h} and two for w_{1h} in Figs. 12 to 14.

G. Higher order MSF with $\boldsymbol{A}$, p-refinement

To cope with problems, where δ is essentially smaller than d, approach (18) is extended. Higher order terms for the laminar part as well as for the edge effect of eddy currents are added [14]. The dimension of the local basis $\mathcal{B}$ is increased, for instance, from one $\mathcal{B}_1 = \{\phi_1\}$ in (18) to two or three $\mathcal{B}_3 = \{\phi_1, \phi_3, \phi_5\}$ leading to the approach of a higher order MSF

$$\tilde{\boldsymbol{A}} = \boldsymbol{A}_0 + \phi_1 \begin{pmatrix} 0 \\ A_1 \end{pmatrix} + \nabla(\phi_1 w_1) + \phi_3 \begin{pmatrix} 0 \\ A_3 \end{pmatrix} + \nabla(\phi_3 w_3) + \phi_5 \begin{pmatrix} 0 \\ A_5 \end{pmatrix} + \nabla(\phi_5 w_5). \tag{23}$$

Since the magnetic flux density $\boldsymbol{B}$ is an even function across the laminates, only odd higher order terms for the MSF with $\boldsymbol{A}$ are considered in (23). The higher order multiscale functions ϕ_3 and ϕ_5, see Fig. 15, are living in Ω_c, i.e. on iron subintervalls. The multiscale functions ϕ_3 and ϕ_5 are equal to zero in air and, thus, represent bubble functions. Therefore, they preserve the required continuity of the tangential component of $\boldsymbol{A}$.

The associated weak form for the higher order multiscale finite element method (HMSFEM) of (23) is a straightforward extension of (19) and, therefore, not shown here. The choice of the FE subspaces $\boldsymbol{A}_{0h} \in \mathcal{U}_h \subset H(\mathrm{curl}, \Omega)$, A_{1h}, A_{3h} and $A_{5h} \in \mathcal{V}_h \subset L_2(\Omega_m)$, w_{1h}, w_{3h} and $w_{5h} \in \mathcal{W}_h \subset H^1(\Omega_m)$ and ϕ_1, ϕ_3 and $\phi_5 \in H_{per}(\Omega_m)$ is obvious.

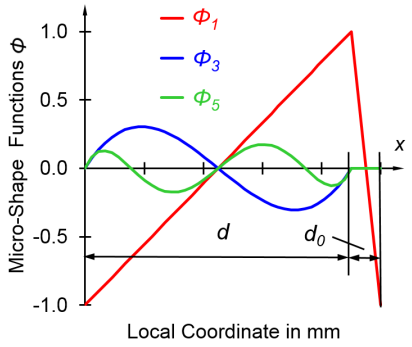

Figure 15: Odd micro-shape functions.

Figures 16 to 18 show results for different dimensions of the local space. Adding of 3^{rd} order terms improves the accuracy enormously. The 5^{th} order approach performs clearly better than the 3^{rd} order one for small δ. The degree of the SFEPs was one for $\boldsymbol{A}_{0h}$, one for A_{1h}, A_{3h} and A_{5h} and two for w_{1h}, w_{3h} and w_{5h}. The computational costs are compared in Table II. A fairly good improvement has been achieved increasing the dimension of the local basis for this small problem.

H. Stability of MSFEM

This section deals with the stability of MSFEM with respect to the degree of SFEPs mainly with $\boldsymbol{A}$ in a particular case. The MSFEM for $\boldsymbol{A}$ in Sec. V with $A_1 \in L_2(\Omega_m)$ offers the opportunity to apply static condensation to the degrees of

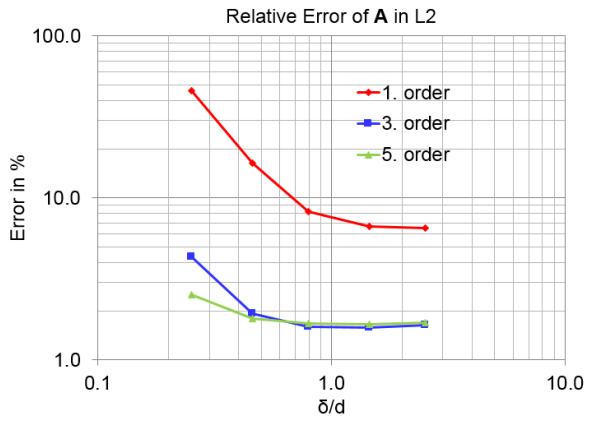

Figure 16: Magnetic vector potential $\boldsymbol{A}$.

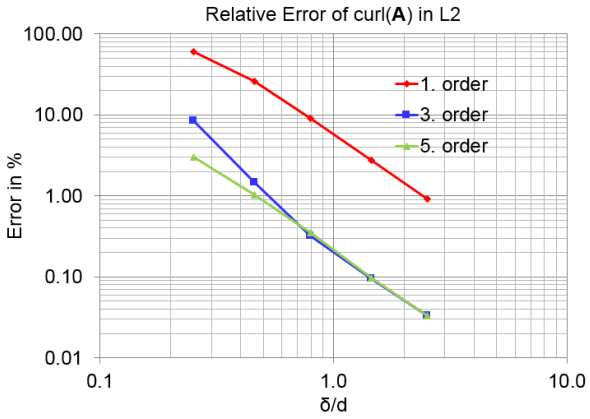

Figure 17: Magnetic flux density curl $\boldsymbol{A}$.

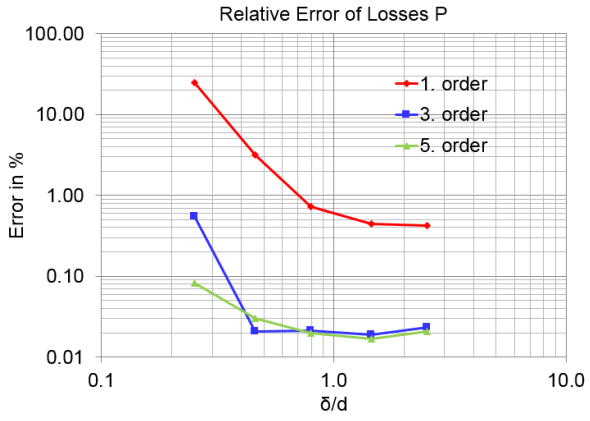

Figure 18: Eddy current losses P.

freedom belonging to L_2 with which the number of unknowns can essentially be reduced. The FE-mesh described in Table I and Fig. 4 has been used for all numerical investigations. One period $p = d + d_0$ equals to 2 mm and fits exactly to one FE-layer on the left and on the right side of Ω_m.

Linear dependence is an important issue of multiscale methods but it is rather seldom addressed [15], [16]. Strictly speaking, the basis of functions $\psi_{ij}(x)$ of the MSFEM (19) are linear

Table II: Number of Degrees of Freedom

	Total No.	$H(\text{curl}, \Omega)$	$L_2(\Omega_m)$	$H^1(\Omega_m)$
RS	24,745 [a])	24,745	-	-
MSFEM	1,675 [b])	676	152 [c])	181 [c])

[a]) For 6^{th} order $H(\text{curl})$ - elements for the smallest δ.
[b]) For the 5^{th} higher order MSF, static condensation eliminates all degrees of freedom of $L_2(\Omega)$ and possible higher order ones of $H(\text{curl}, \Omega)$ and $H^1(\Omega_m)$.
[c]) Holds for one term in approach (23)

independent but not well-conditioned. Contrary to $A_1 \in L_2$ partial derivatives of A_1 are considered in case of $A_1 \in H_1$ introducing some degree of smoothing, compare Figs. 19. Analysis of the FE system matrices showed very similar condition numbers and eigenvalue spectra of both MSFEMs and with averaged coefficients. Surprisingly, the MSFEM with $A_1 \in H^1$ is stable with respect to the degree of SFEPs as can be seen in Figs. 20 to 22. The abscissa shows the degree of the SFEPs of $\boldsymbol{A}_0$ and A_1, that of w_1 is one greater than those. The error for $A_1 \in H^1(\Omega_m)$ decreases slightly with degree of SFEPs whereas that for $A_1 \in L_2(\Omega_m)$ grow rapidly and for the losses in an uncontrolled manner. The method with averaged coefficients indicated with AC is robust against instability.

The same instability can be observed for HMSFEM with A_1, A_3 and $A_5 \in L_2$. Since Dirichlet boundary conditions have to be prescribed for T_2 only $T_2 \in H^1$ is possible. Investigations of MSFEM with T showed no instability.

An effective and simple remedy for the instability is to resolve the outermost laminates by the SFEM while the MSFEM with exact integration is retained for the rest of the laminates. Two laminates (p = 1.0 mm) in each outermost layer is stable up to a polynomial degree of the SFE basis with four for $\boldsymbol{A}_0$ and A_1 and five for w_1.

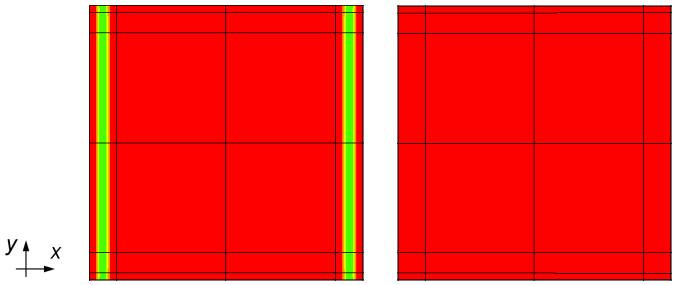

Figure 19: Real part of A_1 in Ω_m for a) $A_1 \in L_2(\Omega_m)$ (right) and b) $A_1 \in H_1(\Omega_m)$ (left).

VI. Large Nonlinear Problem

To demonstrate the ability of MSFEM to cope with large and nonlinear problems and to clearly point out the benefit of the MSFEM compared with the SFEM a large nonlinear problem with FE models in Figs. 23 have been studied. The nonlinear problem with the magnetization curve in Fig. 24 consists of 1,000 laminates. MSFEM of 1^{st} order of (19) has been studied. The implicit Euler method was used for the time discretization and Newton's method to solve the nonlinear problem. The

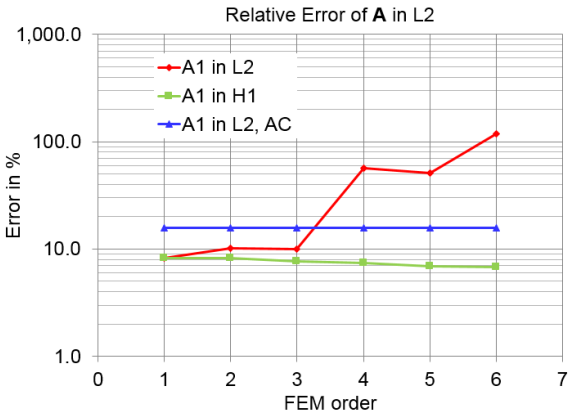

Figure 20: Magnetic vector potential $\boldsymbol{A}$.

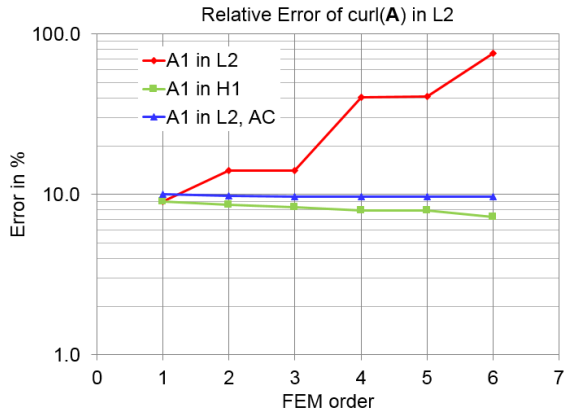

Figure 21: Magnetic flux density curl $\boldsymbol{A}$.

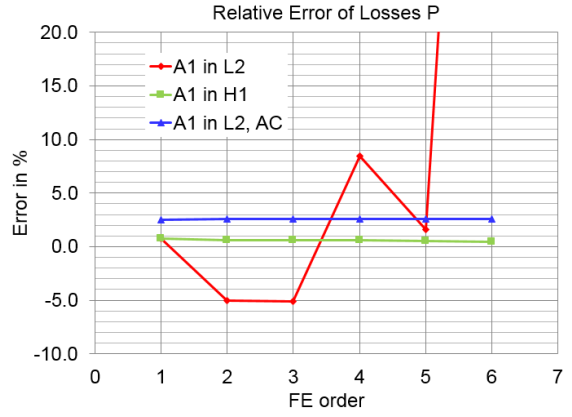

Figure 22: Eddy current losses P.

agreement of the eddy current losses with respect to time in Fig. 25 is very satisfactory. The reduction of computational costs by means of MSFEM compared with SFEM and the RS is impressive as can be seen in Table III. The computational requirements of MSFEM for this large problem and the linear case are almost the same as those for the small problem in Table II, Sec. V-G, for the 1^{st} order MSFEM with only 10 laminates.

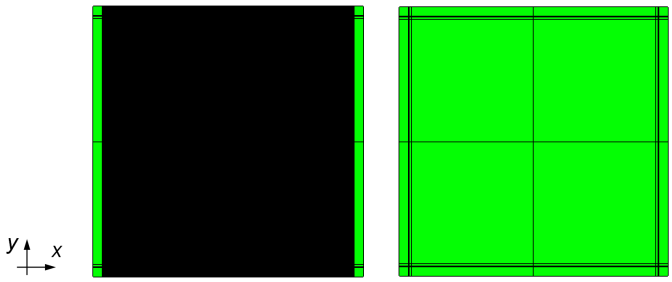

Figure 23: FE models for a) RS (left) and b) MSFEM (right).

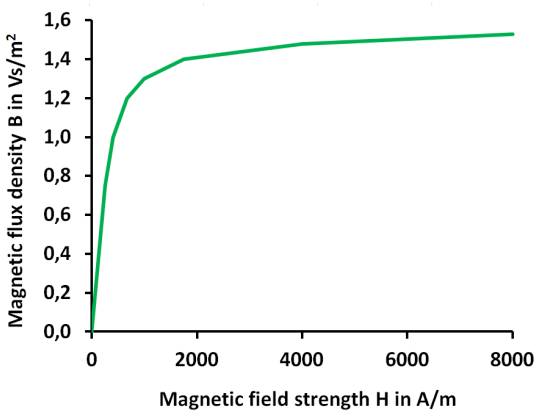

Figure 24: Magnetization curve.

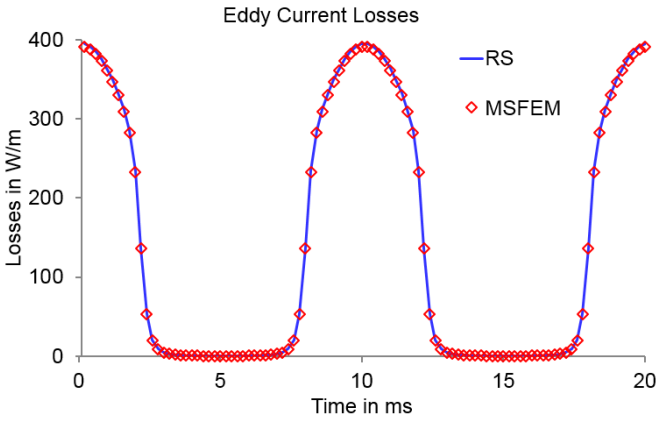

Figure 25: Evolution over time of eddy current losses.

Table III: Number of Degrees of Freedom

	Total No.	$H(\text{curl},\Omega)$	$L_2(\Omega_m)$	$H^1(\Omega_m)$
RS	164, 430	164, 430	-	-
MSFEM	1, 289 [a])	840	208	241

[a]) For the 1^{st} order MSF in (23)

VII. Higher Order Multiscale Finite Element Method with Single Component Current Vector Potential T

A. Boundary value problem with T

The current density $\boldsymbol{J}$ can be represented with a current vector potential $\boldsymbol{T}$ by $\boldsymbol{J} = \text{curl}\,\boldsymbol{T}$. This section deals with the

single component current vector potential T, e.g., pointing in z-direction $\boldsymbol{T} = T\boldsymbol{e}_z$ in the frequency domain:

$$T: \quad \Omega \subset \mathbb{R}^2 \quad \rightarrow \quad \mathbb{C}, \quad (x,y) \mapsto T(x,y) \tag{24}$$

$$\operatorname{curl} T: \quad \Omega \subset \mathbb{R}^2 \quad \rightarrow \quad \mathbb{C}^2, \quad (x,y) \mapsto \begin{pmatrix} \frac{\partial T}{\partial y} \\ -\frac{\partial T}{\partial x} \end{pmatrix}(x,y) \tag{25}$$

A simple BVP of the ECP in the frequency domain reads, see Fig. 3:

$$\operatorname{curl} \frac{1}{\sigma} \operatorname{curl} T + j\mu\omega T = 0 \quad \text{in} \quad \Omega \subset \mathbb{R}^2 \tag{26}$$

$$T = T_0 \quad \text{on} \quad \Gamma \tag{27}$$

B. Weak form with T

The weak form in the frequency domain reads:
Find $T_h \in V_{h,T_0} := \{T_h \in \mathcal{U}_h : T_h = T_0 \text{ on } \Gamma\}$, such that

$$\int_\Omega \frac{1}{\sigma} \operatorname{curl} T_h \cdot \operatorname{curl} t_h \, d\Omega + j\omega \int_\Omega \mu T_h t_h \, d\Omega = 0 \tag{28}$$

for all $t_h \in V_{h,0}$, where $\mathcal{U}_h \subset H^1(\Omega)$.
The solution of (28) serves as RS to evaluate the MSFEM with T.

C. Higher order multiscale finite element method with T

The MSF up to the order 4 for the single component current vector potential

$$\tilde{T}(x,y) = T_0(x,y) + \phi_2(x)T_2(x,y) + \phi_4(x)T_4(x,y) \tag{29}$$

with even micro-shape functions ϕ_2 and ϕ_4 shown in Fig. 26 yields the multiscale current density

$$\tilde{\boldsymbol{J}} = \operatorname{curl} \tilde{T} = \begin{pmatrix} T_{0y} \\ -T_{0x} \end{pmatrix} + \begin{pmatrix} \phi_2 T_{2y} \\ -\phi_{2x} T_2 - \phi_2 T_{2x} \end{pmatrix} + \begin{pmatrix} \phi_4 T_{4y} \\ -\phi_{4x} T_4 - \phi_4 T_{4x} \end{pmatrix}. \tag{30}$$

Simply speaking T corresponds to the magnetic field strength $\boldsymbol{H}$ which is an even function, therefore the multiscale functions ϕ_2 and ϕ_4 are used.

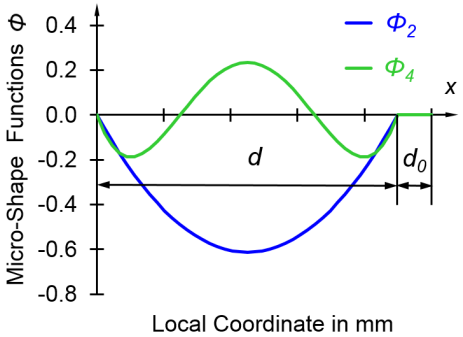

Figure 26: Even micro-shape functions.

D. Weak form of HMSFEM with T

Find $(T_{0h}, T_{2h}, T_{4h}) \in V_{h,T_0} := \{(T_{0h}, T_{2h}, T_{4h}) : T_{0h} \in \mathcal{U}_h, T_{2h} \text{ and } T_{4h} \in \mathcal{V}_h, T_{0h} = T_0 \text{ on } \Gamma \text{ and } T_{2h} = 0 \text{ and } T_{4h} = 0 \text{ on } \Gamma_{m0,1} \subset \Gamma_{m0}\}$, such that

$$\int_\Omega \frac{1}{\sigma} \operatorname{curl} \tilde{T}_h \cdot \operatorname{curl} \tilde{t}_h \, d\Omega + j\omega \int_\Omega \mu \tilde{T}_h \tilde{t}_h \, d\Omega = 0 \tag{31}$$

for all $(t_{0h}, t_{2h}, t_{4h}) \in V_{h,0}$, where $\mathcal{U}_h$ is a subspace of $H^1(\Omega)$, $\mathcal{V}_h$ of $H^1(\Omega_m)$ and ϕ_2 and $\phi_4 \in H^1_{per}(\Omega_m)$.
Homogenous essential boundary conditions are prescribed for $T_2 = 0$ and $T_4 = 0$ on the interface $\Gamma_{m0,1}$ of $\Gamma_{m0} = \Gamma_{m0,1} \cup \Gamma_{m0,2}$, see Fig. 27, to ensure the edge effect that can easily be seen by the y-component in (30).

E. p-refinement of the standard FE basis

This time attention is paid to the accuracy with respect to the degree of the SFEPs, see Figs. 28 to 36. The degree of the SFEPs is one for T_{0h}, T_{2h} and T_{4h} in Figs. 28 to 30, one for T_{0h} and two for T_{2h} and T_{4h} in Figs. 31 to 33 and one for T_{0h} and three for T_{2h} and T_{4h} in Figs. 34 to 36. The errors are visibly reduced by increasing the degree of the SFEPs. The 4^{th} order MSFEM performs clearly better than the 2^{nd} order one. This holds in general for small $\frac{\delta}{d}$ (Figs. 28 to 36) and in particular for the 3^{rd} degree of SFEPs (Figs. 34 to 36).

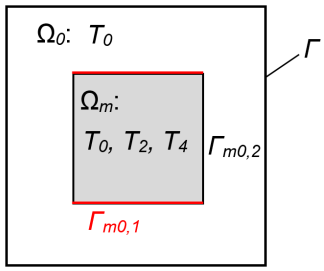

Figure 27: Support, boundary and interface conditions.

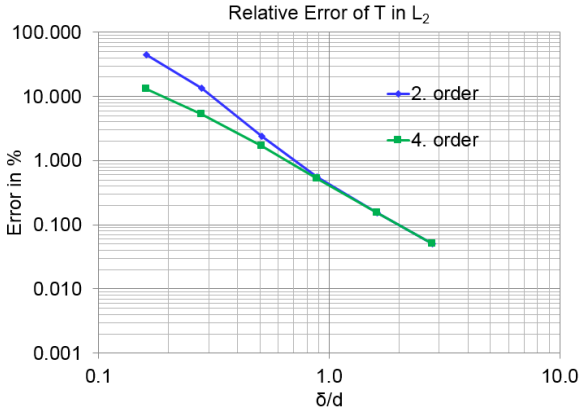

Figure 28: Current vector potential T.

The computational costs are summarized in Table IV. A fairly

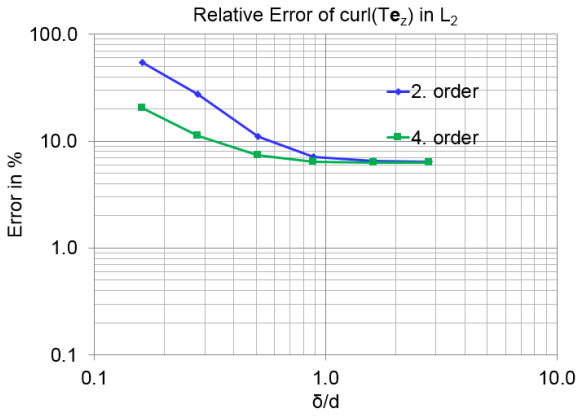

Figure 29: Current density curl T.

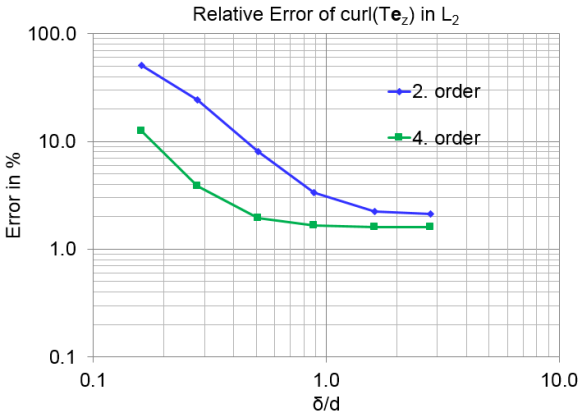

Figure 32: Current density curl T.

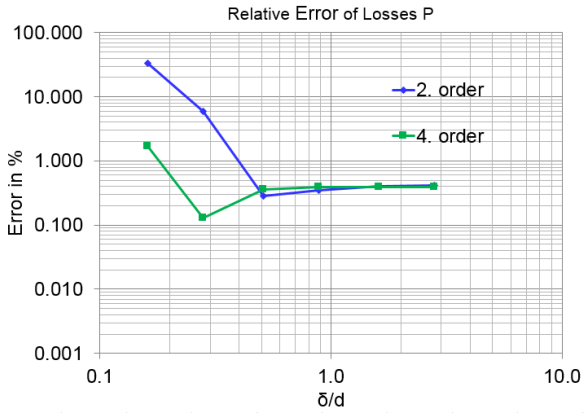

Figure 30: Eddy current losses P.

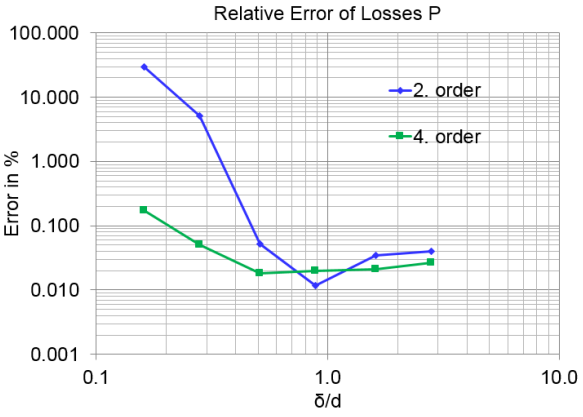

Figure 33: Eddy current losses P.

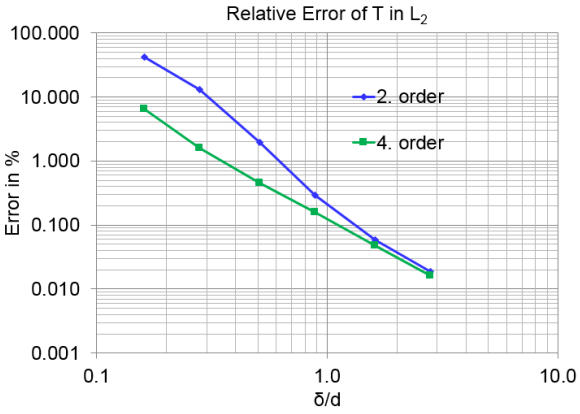

Figure 31: Current vector potential T.

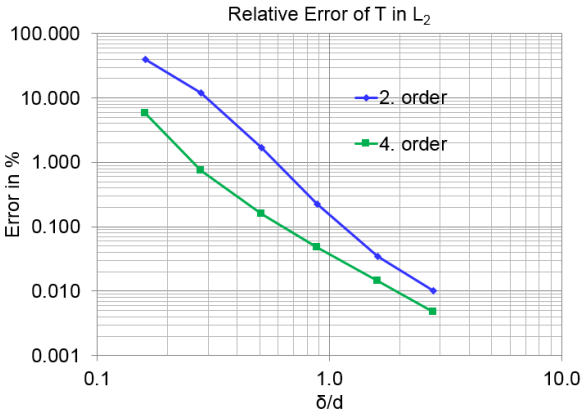

Figure 34: Current vector potential T.

good improvement has been achieved for this small problem.

It is worth mentioning that both the degree of SFEPs and the order of the MSA along with the micro-shape functions can not be increased arbitrarily because of the linear dependence due to the tensor product of MSA (18) and the use of quadrilateral FEs.

F. Edge effect

The difference between considering and neglecting the edge effect is shown by means of eddy currents in Figs. 37. In contrast to MSFEM with $\boldsymbol{A}$ in Sec. V MSFEM with T works also without prescribing homogenous essential boundary conditions for T_2 and T_4 on $\Gamma_{m0,1}$, i.e. without considering the edge effect, reasonably and offers therefore the opportunity to

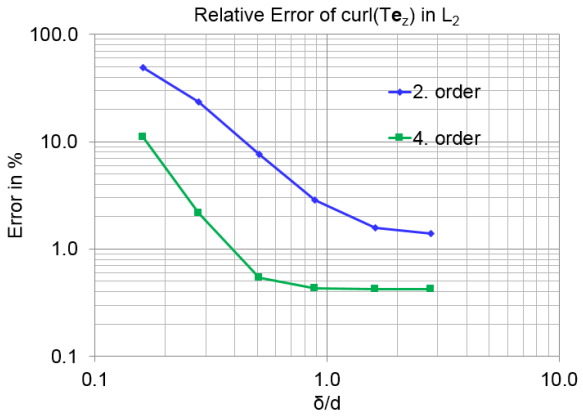

Figure 35: Current density curl T.

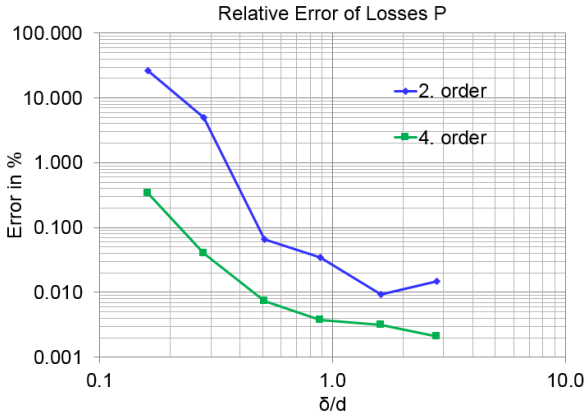

Figure 36: Eddy current losses P.

Table IV: Number of Degrees of Freedom

	Total No.	$H^1(\Omega)$	$H^1(\Omega_m)$	$H^1(\Omega_m)$
RS	9,211	9,211 [a])	-	-
MSFEM	721	99 [b])	311 [c])	311 [d])

[a]) T of 6^{th} order $H^1(\Omega)$-elements for the smallest δ
[b]) T_0 of 1^{st} order $H^1(\Omega_m)$
[c]) T_2 of 3^{rd} order $H^1(\Omega_m)$
[d]) T_4 of 3^{rd} order $H^1(\Omega_m)$

study the influence of the edge effect. Dashed lines in Figs. 38 to 40 stand for edge effect neglected and solid lines for edge effect considered. Note, that the abscissa in all Figs. 38 to 40 represents the thickness d of the laminates and δ was about 0.5mm. The influence of the edge effect can easily be seen.

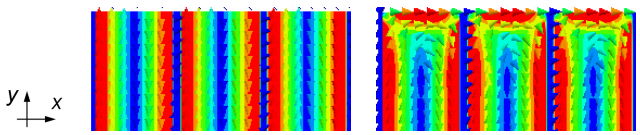

Figure 37: Eddy current distribution a) considering (left) and b) neglecting (right) the edge effect.

The error of curl $T\boldsymbol{e}_z$ neglecting the edge effect is relatively large throughout the range of d. A substantial improvement can be observed considering the edge effect for this small example. In general errors decrease due to the edge effect for smaller d. The 2^{nd} order MSA shows clearly faster growing errors with large d compared to the 4^{th} order one.
The degree of the SFEPs is one for T_{0h} and two for T_{2h} and T_{4h} in Figs. 38 to 40.

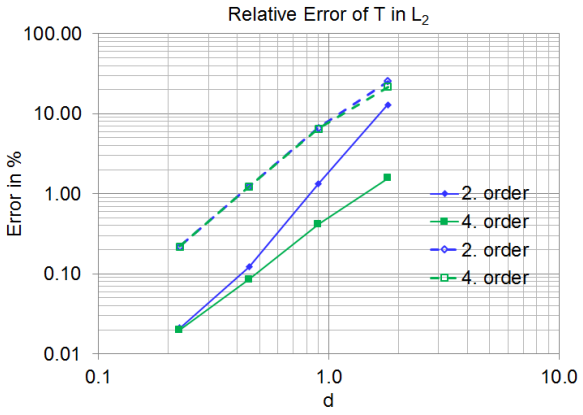

Figure 38: Current vector potential T.

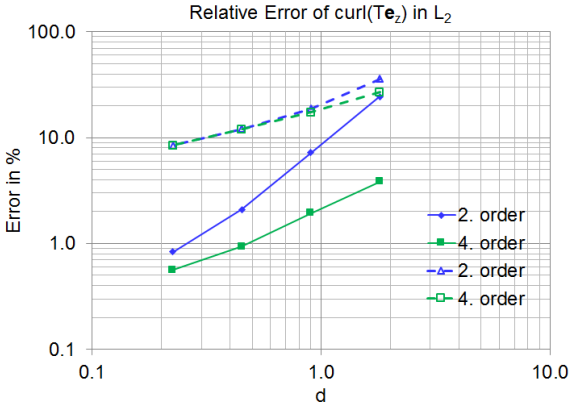

Figure 39: Current density curl T.

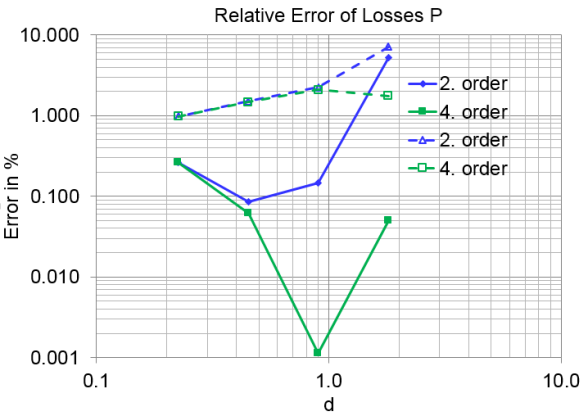

Figure 40: Eddy current losses P.

VIII. Multiscale Finite Element Method with a Mixed Formulation using $(\boldsymbol{A}, \boldsymbol{J})$

Introducing the current density

$$\boldsymbol{J}_h = -j\omega\sigma \boldsymbol{A}_h \tag{32}$$

also as an unknown yields the additional relation

$$-\int_\Omega \boldsymbol{A}_h \cdot \boldsymbol{g}_h \, d\Omega + \frac{j}{\omega}\int_\Omega \frac{1}{\sigma}\boldsymbol{J}_h \cdot \boldsymbol{g}_h \, d\Omega = 0 \tag{33}$$

for the weak form of the mixed formulation:

A. Weak form of the standard mixed formulation with $(\boldsymbol{A}, \boldsymbol{J})$

Find $(\boldsymbol{A}_h, \boldsymbol{J}_h) \in V_{h,\alpha} := \{(\boldsymbol{A}_h, \boldsymbol{J}_h) : \boldsymbol{A}_h \in \mathcal{U}_h, \boldsymbol{J}_h \in \mathcal{M}_h$ and $\boldsymbol{A}_h \times \boldsymbol{n} = \boldsymbol{\alpha}_h$ on $\Gamma\}$, such that

$$\int_\Omega \frac{1}{\mu}\operatorname{curl}\boldsymbol{A}_h \cdot \operatorname{curl}\boldsymbol{v}_h \, d\Omega - \int_\Omega \boldsymbol{J}_h \cdot \boldsymbol{v}_h \, d\Omega = 0 \tag{34}$$

$$-\int_\Omega \boldsymbol{A}_h \cdot \boldsymbol{g}_h \, d\Omega + \frac{j}{\omega}\int_\Omega \sigma\boldsymbol{J}_h \cdot \boldsymbol{g}_h \, d\Omega = 0 \tag{35}$$

for all $(\boldsymbol{v}_h, \boldsymbol{g}_h) \in V_{h,0}$ with $\mathcal{U}_h \subset H(\operatorname{curl}, \Omega)$ and $\mathcal{M}_h \subset H(\operatorname{div}, \Omega)$.

B. Weak form of the mixed multiscale finite element method (MMSFEM) with $(\tilde{\boldsymbol{A}}_h, \tilde{\boldsymbol{J}}_h)$

The approach of the current density

$$\tilde{\boldsymbol{J}} \quad = \quad \boldsymbol{J}_0 + \operatorname{curl}(\phi_2 T_2 \boldsymbol{e}_z) \tag{36}$$

for the MSF has been constructed with the single component current vector potential T_2. Together with (18) for $\boldsymbol{A}$ the weak form of the mixed MSF is obtained:
Find $(\boldsymbol{A}_{0h}, A_{1h}, w_{1h}, \boldsymbol{J}_{0h}, T_{2h}) \in V_{h,\alpha} := \{(\boldsymbol{A}_{0h}, A_{1h}, w_{1h}, \boldsymbol{J}_{0h}, T_{2h}) : \boldsymbol{A}_{0h} \in \mathcal{U}_h, A_{1h} \in \mathcal{V}_h, w_{1h}$ and $T_{2h} \in \mathcal{W}_h, \boldsymbol{J}_{0h} \in \mathcal{M}_h$ and $\boldsymbol{A}_{0h} \times \boldsymbol{n} = \boldsymbol{\alpha}_h$ on $\Gamma\}$, such that

$$\int_\Omega \frac{1}{\mu}\operatorname{curl}\tilde{\boldsymbol{A}}_h \cdot \operatorname{curl}\tilde{\boldsymbol{v}}_h \, d\Omega - \int_\Omega \tilde{\boldsymbol{J}}_h \cdot \tilde{\boldsymbol{v}}_h \, d\Omega \quad = \quad 0 \tag{37}$$

$$-\int_\Omega \tilde{\boldsymbol{A}}_h \cdot \tilde{\boldsymbol{g}}_h \, d\Omega + \frac{j}{\omega}\int_\Omega \frac{1}{\sigma}\tilde{\boldsymbol{J}}_h \cdot \tilde{\boldsymbol{g}}_h \, d\Omega \quad = \quad 0 \tag{38}$$

$$p\int_\Omega \operatorname{div}\boldsymbol{J}_{0h} \operatorname{div}\boldsymbol{g}_{0h} \, d\Omega \quad = \quad 0 \tag{39}$$

for all $(\boldsymbol{v}_{0h}, v_{1h}, q_{1h}, \boldsymbol{g}_{0h}, t_{2h}) \in V_{h,0}$ with $\mathcal{U}_h \subset H(\operatorname{curl}, \Omega)$, $\mathcal{V}_h \subset L_2(\Omega_m)$, $\mathcal{W}_h \subset H^1(\Omega_m)$, $\mathcal{M}_h \subset H(\operatorname{div}, \Omega)$ and ϕ_1 and $\phi_2 \in H^1_{per}(\Omega_m)$ and for a sufficiently large $p \in \mathbb{R}$. The micro-scale currents in (36) are divergence free per se. To get also a divergence free macro-scale current density $\boldsymbol{J}_{0h}$ and a unique solution the penalty term in (39) is additionally required.
The computational costs of the mixed formulation are certainly higher than that of the corresponding standard formulation with $\boldsymbol{A}$. However, the mixed formulation performs much better in reproducing the edge effect as can easily be seen in Fig. 41. A comparison of the losses obtained by different methods are shown in Fig. 42. The error of the MMSFEM and that of the mixed SFEM are practically identical and are enclosed by those of the MSFEM of 1^{st} with $\boldsymbol{A}$ order as upper bound and those of the MMSFEM with $(\tilde{\boldsymbol{A}}_h, \tilde{\boldsymbol{J}}_h)$ of 2^{nd} order as lower bound. The degrees of the SFEPs are one for $\boldsymbol{A}_{0h}$, A_{1h} and $\boldsymbol{J}_{0h}$ and two for w_{1h} and T_{2h}.

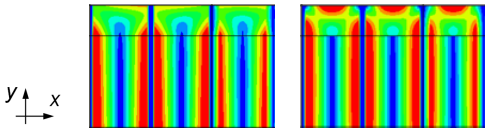

Figure 41: Edge effect by means of the current density: a) MSFEM with $\tilde{\boldsymbol{A}}_h$ (left) and b) MMSFEM with $(\tilde{\boldsymbol{A}}_h, \tilde{\boldsymbol{J}}_h)$ (right).

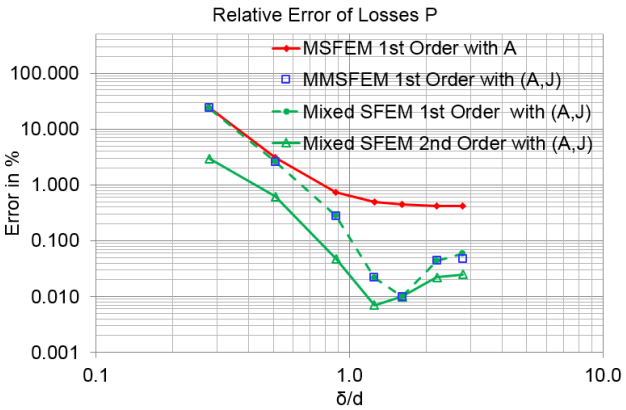

Figure 42: Eddy current losses P of mixed formulations with $(\tilde{\boldsymbol{A}}_h, \tilde{\boldsymbol{J}}_h)$ and of the MSFEM with $\boldsymbol{A}$.

Acknowledgment

This work was supported by the Austrian Science Fund (FWF) under Project P 27028-N15.

References

[1] A. De Rochebrune, J. Dedulle, and J. Sabonnadiere, "A technique of homogenization applied to the modelling of transformers," *IEEE Trans. Magn.*, vol. 26, no. 2, pp. 520 –523, March 1990.

[2] A. Bensoussan, J. Lions, and G. Papanicolaou, *Asymptotic Analysis for Periodic Structures*. North-Holland, 2011.

[3] D. Cioranescu and P. Donato, *An Introduction to Homogenization*. Oxford University Press, 1999.

[4] P.-S. Shin and J. Lee, "Magnetic field analysis of amorphous core transformer using homogenization technique," *IEEE Trans. Magn.*, vol. 33, no. 2, pp. 1808 –1811, March 1997.

[5] O. Bottauscio, M. Chiampi, and A. Manzin, "Computation of higher order spatial derivatives in the multiscale expansion of electromagnetic-field problems," *IEEE Trans. Magn.*, vol. 44, no. 6, pp. 1194–1197, 2008.

[6] P. Dular, J. Gyselinck, and L. Krähenbühl, "A time-domain finite element homogenization technique for lamination stacks using skin effect sub-basis functions," *COMPEL*, vol. 25, no. 1, pp. 6–16, 2006.

[7] K. Hollaus and J. Schöberl, "Homogenization of the eddy current problem in 2D," ser. 14th Int. IGTE Symp., Graz, Austria, Sep. 2010, pp. 154–159.

[8] J. Schöberl and S. Zaglmayr, "High order Nédélec elements with local complete sequence properties," *COMPEL*, vol. 24, no. 2, pp. 374–384, 2005.

[9] I. Babuska and J. M. Melenk, "The partition of unity method," *Int. J. Numer. Meth. Engng.*, vol. 40, pp. 727–758, 1997.

[10] T. Strouboulis, K. Copps, and I. Babuska, "The generalized finite element method: an example of its implementation and illustration of its performance," *Int. J. Numer. Meth. Engng.*, vol. 47, pp. 1401–1417, 2000.

[11] P. Ledger and S. Zaglmayr, "hp-finite element simulation of three-dimensional eddy current problems on multiply connected domains," *Computer Methods in Applied Mechanics and Engineering*, vol. 199, no. 49-52, pp. 3386–3401, 2010.

[12] P. Dular, "A time-domain homogenization technique for lamination stacks in dual finite element formulations," *J. Comput. Appl. Math.*, vol. 215, no. 2, pp. 390–399, 2008.
[13] K. Hollaus, A. Hannukainen, and J. Schöberl, "Two-scale homogenization of the nonlinear eddy current problem with FEM," *IEEE Trans. Magn.*, vol. 50, no. 2, pp. 413–416, Feb 2014.
[14] K. Hollaus and J. Schöberl, "A higher order multi-scale FEM with A for 2D eddy current problems in laminated iron," *IEEE Trans. Magn.*, vol. 51, no. 3, 2015.
[15] A.-M. Matache, I. Babuska, and C. Schwab, "Generalized p-FEM in homogenization," *Numerische Mathematik*, vol. 86, no. 2, pp. 319–375, 2000.
[16] R. Tian, G. Yagawa, and H. Terasaka, "Linear dependence problems of partition of unity-based generalized fems," *Computer Methods in Applied Mechanics and Engineering*, vol. 195, no. 37, pp. 4768 – 4782, 2006.

Appendix A
Some Equations

$$\int_\Omega \frac{1}{\mu}\,\mathrm{curl}\left(\boldsymbol{A}_{0h}+\phi_1\begin{pmatrix}0\\A_{1h}\end{pmatrix}\right)\cdot\mathrm{curl}\left(\boldsymbol{v}_{0h}+\phi_1\begin{pmatrix}0\\v_{1h}\end{pmatrix}\right)d\Omega+j\omega\int_\Omega\sigma\left(\boldsymbol{A}_{0h}+\phi_1\begin{pmatrix}0\\A_{1h}\end{pmatrix}+\nabla(\phi_1 w_{1h})\right)\cdot\left(\boldsymbol{v}_{0h}+\phi_1\begin{pmatrix}0\\v_{1h}\end{pmatrix}+\nabla(\phi_1 q_{1h})\right)d\Omega=0 \tag{20}$$

$$\int_\Omega\begin{pmatrix}\mathrm{curl}\,\overline{\boldsymbol{A}}_{0h}\\\overline{A}_{1h}\end{pmatrix}^T\begin{pmatrix}\overline{\nu} & \overline{\nu\phi_{1x}}\\ \overline{\nu\phi_{1x}} & \overline{\nu\phi_{1x}^2}\end{pmatrix}\begin{pmatrix}\mathrm{curl}\,\overline{\boldsymbol{v}}_{0h}\\\overline{v}_{1h}\end{pmatrix}d\Omega+j\omega\int_\Omega\begin{pmatrix}(\overline{\boldsymbol{A}}_{0h})_x\\(\overline{\boldsymbol{A}}_{0h})_y\\\overline{A}_{1h}\\\overline{w}_{1hx}\\\overline{w}_{1hy}\end{pmatrix}^T\begin{pmatrix}\overline{\sigma} & 0 & 0 & \overline{\sigma\phi_{1x}} & \overline{\sigma\phi_1} & 0\\ 0 & \overline{\sigma} & \overline{\sigma\phi_1} & 0 & 0 & \overline{\sigma\phi_1}\\ 0 & \overline{\sigma\phi_1} & \overline{\sigma\phi_1^2} & 0 & 0 & \overline{\sigma\phi_1^2}\\ \overline{\sigma\phi_{1x}} & 0 & 0 & \overline{\sigma\phi_{1x}^2} & \overline{\sigma\phi_{1x}\phi_1} & 0\\ \overline{\sigma\phi_1} & 0 & 0 & \overline{\sigma\phi_{1x}\phi_1} & \overline{\sigma\phi_1^2} & 0\\ 0 & \overline{\sigma\phi_1} & \overline{\sigma\phi_1^2} & 0 & 0 & \overline{\sigma\phi_1^2}\end{pmatrix}\begin{pmatrix}(\overline{\boldsymbol{v}}_{0h})_x\\(\overline{\boldsymbol{v}}_{0h})_y\\\overline{v}_{1h}\\\overline{q}_{1h}\\\overline{q}_{1hx}\\\overline{q}_{1hy}\end{pmatrix}d\Omega=0 \tag{22}$$

Appendix B
Multiscale Finite Element Method Solutions

Typical solutions are selected to make the advantage of MSFEM over standard FEM quite clear. In this context it is worth mentioning that the corresponding solutions of the 3^{rd} order approach are almost the same. Results with the 5^{th} order MSF are shown in Figs. 43 to 44.

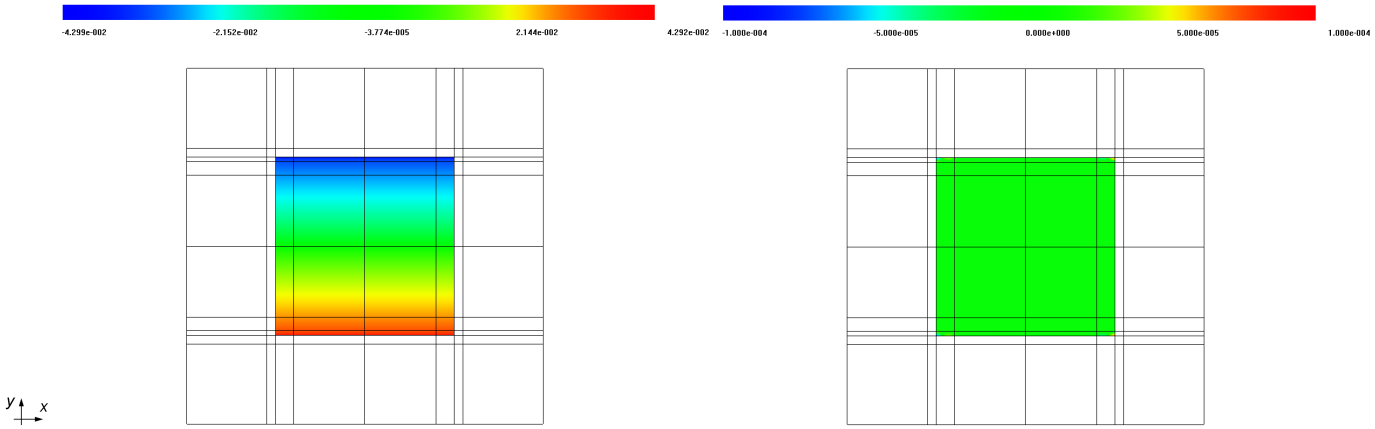

Figure 43: MSFEM solution: $Re(\boldsymbol{A}_{0h}(1))$ (left), $Re(\boldsymbol{A}_{0h}(2))$ (right).

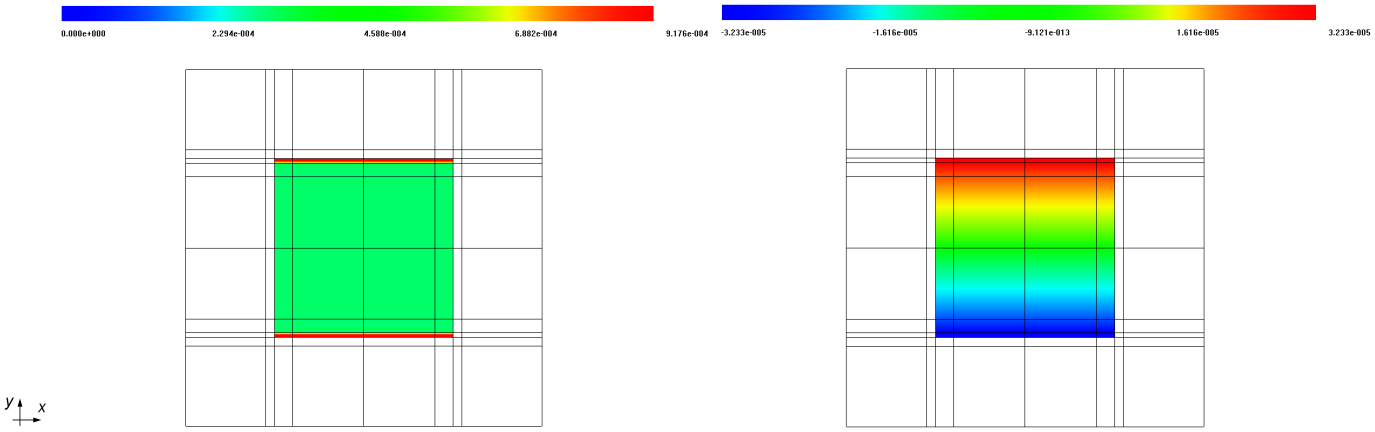

Figure 44: MSFEM solution: $Re(A_{1h})$ (left), $Re(w_{1h})$ (right).